

Contrasting $\text{Pr}_{1-x}\text{Ca}_x\text{MnO}_3$ OER Catalysts with Different Valences and Covalences

Gaurav Lole, Fatemeh Ebrahimi, Tobias Meyer, Daniel Mierwaldt, Vladimir Roddatis, Janis Geppert, Marcel Risch, and Christian Jooss*



Cite This: *J. Phys. Chem. C* 2023, 127, 177–186



Read Online

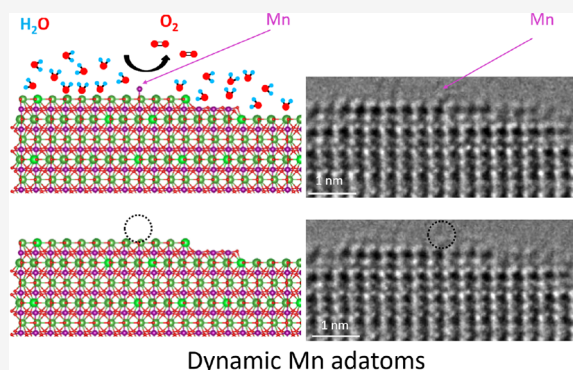
ACCESS |

Metrics & More

Article Recommendations

Supporting Information

ABSTRACT: Perovskite oxides are promising materials for catalyzing the oxygen evolution reaction (OER). However, understanding the properties of active sites that enable high OER activity without corrosive electrode reduction is still elusive. In this work, we use combined electrochemical and environmental transmission electron microscopy (ETEM) studies to compare the OER stability of the (001) surfaces of $\text{Pr}_{1-x}\text{Ca}_x\text{MnO}_3$ perovskite films with doping of $x = 0.1$ and $x = 0.33$. Notably, electrochemical analysis in alkaline conditions, as well as ETEM studies in H_2O vapor, shows parallel trends in the stability of both systems: Mn leaching for the $\text{Pr}_{1-x}\text{Ca}_x\text{MnO}_3$ (PCMO) $x = 0.33$ system due to oxygen vacancy formation at the surface and higher stability of PCMO $x = 0.1$, where the oxygen vacancy redox peak is absent in cyclic voltammetry. Electron energy loss spectroscopy reveals the preservation of the Mn valence state in H_2O for the PCMO $x = 0.1$ system, whereas for $x = 0.33$, Mn is reduced. We interpret this enhanced stability for the low-doped system in terms of a modified Mn 3d–O 2p hybridization, i.e., covalence. For a system with charge localization due to Jahn–Teller polarons, the covalence determines to what degree redox processes of lattice oxygen can arise that can finally lead to corrosive oxygen vacancy formation.



INTRODUCTION

Electrochemical catalytic water splitting, including oxygen evolution, is an eco-friendly and sustainable approach to producing hydrogen with zero carbon emission.¹ The electrocatalytic splitting of water includes the oxygen evolution reaction (OER) ($4\text{OH}^- \rightarrow \text{O}_2 + 2\text{H}_2\text{O} + 4\text{e}^-$) at the anode and the hydrogen evolution reaction (HER) ($2\text{H}_2\text{O} + 2\text{e}^- \rightarrow 2\text{OH}^- + \text{H}_2$) at the cathode. The OER incorporates a four-electron transfer process, which needs a high electric potential to overcome rate-limiting thermodynamic and kinetic energy barriers, depending on the reaction mechanism.^{1–8} In particular, multiple transfer of electrons and protons during the OER result in a higher overpotential in contrast to HER. The utilization of an efficient OER electrocatalyst is, thus, crucial to significantly reduce the overpotential of the anodic reaction in water splitting for hydrogen generation.⁹

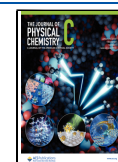
At present, ruthenium (Ru) or Ru-based catalysts have one of the lowest overpotentials for OER under an acidic environment.^{10,11} Iridium (Ir) and Ru-based perovskites are profoundly tuneable and distinct materials that ensure OER electrocatalysis, with many modifications promoting high activities and stabilities in acidic environments. Thus, the noble metal oxides IrO_2 and RuO_2 are presently considered two of the best OER catalysts.¹² However, their high price and low abundance limit the practical utilization of these noble-

metal-based catalysts on a large scale. Therefore, searching for cost-effective alternatives for noble metal catalysts is essential.^{1,3,13,14} Lately, 3d transition-metal oxides (TMOs) have come forth as potential substitutes for RuO_2 and IrO_2 because of their notable activities and low cost in alkaline conditions.^{15–17} Among them, perovskites with the ABO_3 formula have attracted particular attention because of their tuneable structure and properties.^{18–23} Substituting A and B cations alters the electronic structure, oxidation state, and catalytic properties. This substitution permits controlling the valence states of the B-site transition metals and influences the formation of oxygen vacancies.¹ Sometimes, a fast surface reconstruction appears after a few OER cycles or even upon immersion in the electrolyte before initiating the OER process.^{7,24–27} Although many transition-metal perovskite oxides initially show a high catalytic performance, the electrode surface–electrolyte interface reactions and catalyst stability are still difficult to interpret. The perovskite interface to water is

Received: August 7, 2022

Revised: November 17, 2022

Published: December 21, 2022



typically dynamic, showing reversible as well as irreversible processes under OER conditions.²⁸ The most typical irreversible surface transformation occurs due to A-site and B-site transition-metal cations leaching during the OER, which can be facilitated by oxygen vacancy formation and subsequent reduction of the metal species. Leaching of A-site or B-site elements at the electrode surface during the OER leads to a drastic change in OER activity.^{20,28} The underlying mechanisms that control whether the emerging surface processes are reversible or irreversible are still elusive.

One important aspect is the participation of lattice oxygen in the formation of molecular oxygen in some perovskite systems, known as the lattice oxygen mechanism (LOM). This reaction pathway can decrease the energy barrier and leads to higher activity in some perovskite systems.^{20,29,30} On the other hand, the single-site adsorbate evolution mechanism (AEM) typically involves four-step proton–electron transfer reactions occurring entirely on a single B-site metal ion. Based on a frozen surface approximation, a scaling relation between the adsorption energies of the different surface intermediates was proposed.³¹ The DFT calculations reveal an adsorption process that involves antibonding e_g orbitals of TM hybridized with the oxygen 2p bands of oxygen-containing intermediate chemical species. Involving lattice oxygen to couple an O–O bond to produce an O₂ molecule could lower the energy barrier compared to the scaling relation predicted by the AEM because LOM circumvents the formation of the HOO* intermediate. An increase in metal–oxygen covalence is considered a tool for altering the OER mechanism from the AEM to the LOM.²³ Optimizing the e_g filling or increasing the TM 3d–O 2p covalence can boost the OER on the perovskite surface.^{32–35} Thus, optimizing valence and covalence can induce a higher density of the TM 3d acceptor states near the Fermi level and facilitate the electron transfer from the oxygen intermediates to the electrode surface.⁹ By an increase in covalence, the electron transfer between TM ions and oxygen is facilitated, and direct O–O bonding with the reversible formation of oxygen vacancy, i.e., the LOM mechanism, becomes favorable.³⁶

An increased covalence give rises not only to lattice oxygen redox activity but also to the irreversible formation of oxygen vacancies during OER, as observed in refs 37 and 38 for Pr_{1-x}Ca_xMnO₃ (PCMO). Oxygen vacancies modify the electrical conductivity of the surface, alter the electronic structure and transition-metal valence, and can modify the active sites for electrocatalytic reactions.²⁸ However, examples where oxygen vacancies improve OER activity without hampering the stability of the electrode are very rare. One example is the Ruddlesden–Popper La_{0.5}Sr_{1.5}Ni_{1-x}Fe_xO_{4-δ}, where doping-dependent oxygen vacancy formation energy and oxygen mobility together with the capability to insert excess oxygen may result in a stable LOM mechanism.³⁹ More frequently, catalyst corrosion by oxygen vacancies is observed, which can even lead to surface amorphization of perovskites.²⁶ Nevertheless, the impact of oxygen vacancies on the OER activity is still unresolved.

Environmental transmission electron microscopy (ETEM) is a versatile tool for the study of surface changes by the formation of oxygen vacancies due to its high spatial resolution as well as capability of carrying out electron energy loss spectroscopy (EELS) on the catalyst surface.⁴⁰ In differentially pumped systems, the reactive gas is allowed to flow over the surface. Aberration-corrected ETETM studies offer the

possibility of observing the catalyst's surface with real space atomic resolution in several millibars of pressure of reactive gases.⁴¹ The latest advances in atomic resolution observations allow the comparison of surface atomic dynamics in a reactive and inert atmosphere.^{28,42} Developments toward controlling electron beam-induced and applied electric potentials in ETETM enable in situ studies of catalyst surfaces under OER-relevant potentials.²⁸ The capability to regulate the gas pressure during ETETM observations is a beneficial way of exploring changes in the structure and electronic properties.⁴³

In this work, we present an in situ ETETM study of the PCMO manganite system with Ca doping of $x = 0.1$ and $x = 0.33$. We observe a pronounced difference in OER stability both in rotating ring-disk electrode (RRDE) experiments and in ETETM. While PCMO $x = 0.33$ displays a drastic decrease in the OER activity even though it initially shows a high OER current density,²⁸ PCMO $x = 0.1$ has a lower activity, but the decrease is less. EELS analysis shows that the $x = 0.1$ system preserves the Mn³⁺ valence state during OER. In contrast, the $x = 0.33$ system shows surface reduction due to oxygen vacancy formation and subsequent leaching of the formed Mn²⁺ species. For the PCMO $x = 0.1$ system, we also compare two different surfaces, i.e., (001) and (112), which are stable but display quite different surface dynamics. These observations allow us to derive conclusions on the impact of covalence and surface orientation on the dynamic states of the electrode interface to water.

METHODS

Thin Film Fabrication. Pr_{1-x}Ca_xMnO₃ ($x = 0.1$ and $x = 0.33$) films were prepared by ion-beam sputtering (IBS). In the first step, a La_{0.6}Sr_{0.4}MnO₃ (LSMO) layer of 21(2) nm thickness was deposited at 750 °C onto disk-shaped 0.5 wt % Nb-doped SrTiO₃ (STNO) substrates with a (100) orientation (CrysTec GmbH, Berlin, Germany). In the second step, PCMO films were sputtered at 650 °C without exposure to air. The chamber contained 3×10^{-4} mbar Ar and 1.6×10^{-4} mbar O₂ as the reactive gas. Supporting Figure S1 confirms the epitaxial growth of both films. Film thicknesses were measured by X-ray reflectometry (XRR).

Electrochemistry. Electrochemical measurements are performed in an Interface 1000E bipotentiostat setup (Gamry Instruments Inc., Warminster, PA, United States) and an RRDE-3A rotator (ALS Co. Ltd., Tokyo, Japan). PCMO/INSTO electrodes are prepared for an RRDE disk electrode with a diameter of 4 mm and a Pt ring electrode with an inner diameter of 5 mm and an outer diameter of 7 mm. All electrochemical reactions are performed in an 0.1 M KOH electrolyte. The electrolyte solution is prepared by diluting the KOH stock solution (Sigma-Aldrich, Munich, Germany) with deionized water (Milli-Q, >16.5 MΩ). The 0.1 M KOH electrolyte is saturated with argon (Ar) gas at least 30 min before measurements and continuously purged with Ar during the measurements. Electrode potentials are converted to the reversible hydrogen electrode (RHE) scale using $E_{\text{RHE}} = E_{\text{applied}} + E_{\text{ref}}$, where $E_{\text{ref}} = 0.993$ V vs SCE is obtained from the hydrogen evolution using a clean Pt disk. The measured potentials are corrected for the ohmic resistance extracted from the impedance spectroscopy measurement prior to measurement. Cyclic voltammograms are obtained at 10 mV/s with a rotation of 1600 rpm.

Environmental TEM Experiments. In situ ETETM experiments are performed using an FEI Titan ETETM G2 at

80–300 kV. A Cs corrector and Gatan (GIF) Quantum 965ER image filter facilities are attached to the microscope for HRTEM imaging and EELS, respectively. A Gatan UltraScan 1000XP CCD is used to create movies with frame rates between 3 and 4 frames per second (fps) in 512×512 pixels for PCMO $x = 0.33$ and 1024×1024 pixels for PCMO $x = 0.1$, respectively. ETEM is used to capture movies in different ambients, i.e. in high vacuum (HV; $\sim 10^{-5}$ Pa), where the H_2O partial pressure in the octagon is reduced by a cold trap, 100 Pa O_2 , and 0.5–1 Pa H_2O . All time-sequenced HRTEM movies are recorded at a beam current of 4 nA and beam diameters between 145 and 200 nm. Local electron dose rates at the location of the TEM lamella surface are calculated by calibrated CCD contrast with 0.16696 electrons/count, yielding between 8000 and 15,000 $\text{e}/\text{\AA}^2 \text{ s}$ for HV, O_2 , and H_2O surface studies, respectively.

Electron Energy Loss Spectroscopy. The EELS analysis is carried out using a Gatan Quantum 965ER post-column energy filter in ETEM. Mn L and O K edges are recorded using 0.1 eV/ch dispersion in post 1 mbar O_2 and post 8 μbar H_2O . The background is subtracted using power-law background functions from Gatan's DigitalMicrograph fitted to a 50 eV wide window before each Mn L edge and to a 25 eV wide window before each O K edge. EELS analysis and discussion of PCMO $x = 0.33$ can be found in ref 28 as well as in the Supporting Information.

Method of Mn Valence Analysis. Mn valence is calculated by the Mn L_3/L_2 integrated intensity ratio using the same method described in detail by Varela et al.⁴⁴ A 50 eV wide window is used in the power-law background (inbuilt Gatan DM function) to fit before each Mn L_3 edge. A Hartree–Slater (HS) type cross-section step function (in Gatan DigitalMicrograph) is used for subtracting the background inside the L_3 and L_2 edges. The HS step function removes the continuum background contribution of a 10 eV window immediately after the L_2 edge. The high-loss spectrum is calibrated using the energy calibration of the zero-loss peak. The error bars are determined by performing the integration of L_3 and L_2 edges by shifting the integration windows by ± 1 eV.

TEM Lamella Preparation. TEM lamellae for PCMO $x = 0.1$ are prepared from epitaxially grown (001)-oriented thin films by the focused ion-beam lift-out technique using a noble-metal-free protection layer and careful low-energy ion milling for the preparation of ultrathin lamellae. Supporting Figure S2 shows the before and after thinning steps of the PCMO $x = 0.1$ TEM lamella. The lamella preparation is followed by the method explained for the lamella preparation of PCMO $x = 0.33$ in ref 28. Ar ion milling (Precision Ion Polishing System (PIPS) II, Gatan, Inc.) is used for fine thinning and surface cleaning with a 0.3 keV beam energy and a 24.13 μA beam current with only one stationary beam and stage rotation off (stage tilt $\pm 5^\circ$). As reported earlier,^{28,42} the perovskite structure damaged by FIB and PIPS can be recrystallized in high partial pressure O_2 in ETEM. The PCMO $x = 0.1$ reduced surface is recrystallized in 1 mbar O_2 in ETEM. Supporting Figure S3 and Movie M1 show the recrystallization process of the PCMO $x = 0.1$ (001) surface.

Image Simulations. Multi-slice HRTEM image simulation for both PCMO systems is performed with QSTEM⁴⁵ software using a crystal model in which the placement of the mixed A-site atoms, i.e., Pr and Ca, is done column by column. For each atomic site, a Pr atom is set if the fraction of all previously set atoms exceeds the doping concentration x . A Ca atom is placed

otherwise. This way, agglomeration of A-site atoms of the same kind is avoided in each column, and the resulting A-site contrasts are rather homogeneous, matching the experimental observations.

To approximate the experimental conditions for PCMO $x = 0.33$, a small image section is extracted from the experimental data close to the surface and the sample thickness as well as the lens aberrations (including defocus, spherical aberration, two-fold astigmatism, and axial coma) are fitted by minimizing the root-mean-square difference between experimental and simulated images. The Metropolis method is employed as a minimization algorithm, and the virtual temperature is decreased exponentially as a function of the iteration step. PCMO $x = 0.33$ crystal model creation, as well as fitting procedure, was already reported and performed in ref 28.

The main goal of this work is to understand the contrast difference between A- and B-site atomic columns. Therefore, only thickness and defocus parameters are used for the PCMO $x = 0.1$ system and adjusted by hand. The (001) and the (112) surface are simulated without additional lens aberration parameters. The resulting image adequately provides a contrast difference between A-site (Pr/Ca–O) and B-site (Mn–O) atomic columns. The resulting electron optical parameters and sample thickness are noted in Table S1.

RESULTS AND DISCUSSION

Electrochemistry. A cyclic voltammetry (CV) study in an RRDE setup was carried out to study the current density with voltage cycling of epitaxial (001)-oriented $\text{Pr}_{(1-x)}\text{Ca}_x\text{MnO}_3$ thin films at $x = 0.1$ and $x = 0.33$. The structural characterization of both films by XRD and AFM is shown in Supporting Information Figures S1 and S4, respectively. Figure 1a depicts the 2nd and 50th cycles of the CV for both doping in O_2 -saturated 0.1 mol KOH. Both films show exponentially increasing currents that indicate the electrocatalytic activity of OER. In order to qualitatively probe the oxygen produced by the PCMO thin films, additional measurements were performed in Ar-saturated 0.1 mol KOH, where a potential of 0.5 V vs RHE is applied to the Pt ring electrode in order to drive the oxygen reduction reaction (ORR) in transport limitation.⁴⁶ The ring current densities show the same exponential trend as the disk current densities (Supporting Figure S5). This supports the assignment of the disk current to the evolution of oxygen. Clearly, for $x = 0.33$, the onset of OER occurs at a lower potential, demonstrating a higher activity compared to $x = 0.1$, which decreases for both samples upon cycling.

Additionally, a cathodic redox transition peak is visible on PCMO for $x = 0.33$ at $E = 1.3$ V vs RHE. During cycling, the corresponding anodic peak becomes visible (50th cycle, indicated by an arrow). The redox couple is related to the reversible formation and annihilation of oxygen vacancies, which are electron donors and thus induce surface reduction of the transition metal.³⁷ The easy formation of oxygen vacancies in the PCMO film with $x = 0.33$ suggests that lattice oxygen is redox-active; i.e., holes can be transferred between Mn 3d and O 2p states. They can oxidize O^{2-} to form O^- and $\text{O}_2(\text{g})$.²⁸ This feature was not observed in the PCMO $x = 0.1$ film. As a result, the CV of this film did not show any pre-catalytic redox peaks.

In order to study the stability of both doping levels, chronoamperometric measurements of the OER current have been performed. Figure 1b,c compares the time decays of the

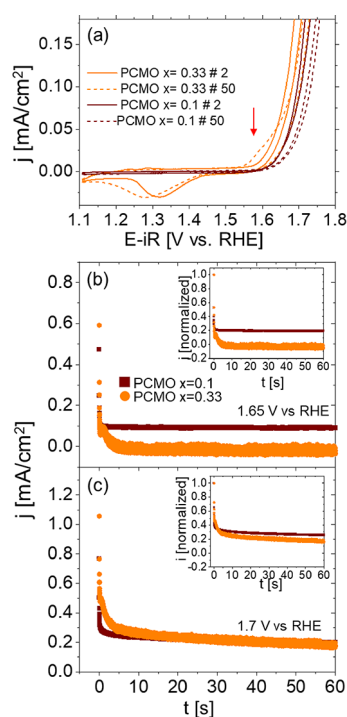


Figure 1. Electrochemical OER performance of epitaxial PCMO $x = 0.1$ and $x = 0.33$ (001)-oriented thin films. (a) Cyclic voltammograms of both films at cycles 2 and 50. In addition to the OER, PCMO $x = 0.33$ shows a redox couple after 50 cycles as indicated by an arrow. Chronoamperometric measurements show the current at two applied potentials of (b) 1.65 V vs RHE and (c) 1.7 V vs RHE as a function of time in an argon-saturated electrolyte. The insets show normalized plots of panels (b) and (c).

catalytic current densities of the two electrodes in Ar-saturated conditions. After an initial fast drop, the current remains more stable for the $x = 0.1$ sample compared to that for $x = 0.33$, which has a higher initial absolute current density (Figure 1b). The chronoamperometric measurements for higher applied potentials up to 1.8 V vs RHE and for O_2 -saturated conditions are shown in Supporting Figures S6 and S7. Remarkably, at higher anodic polarization (Figure 1c) as well as for O_2 saturation, the difference in time decay between the two doping levels almost disappears. This points to a loss of lattice oxygen and vacancy formation as a dominant corrosion mechanism for the $x = 0.33$ films, which is minor at higher anodic potentials and electrolyte oxygen concentrations. AFM images of as-grown epitaxial films before and after electrochemical measurement do not reveal significant changes in the microstructure of the surfaces after cycling (see Supporting Figure S4).

Termination of PCMO $x = 0.1$ and $x = 0.33$ (001) Surfaces. Surface termination of the (001) surfaces of PCMO $x = 0.1$ and 0.33 is observed by ETEM in different reactive (H_2O and O_2) and inert (HV) environments. The study of surface termination is performed on the HRTEM images recorded in negative defocus; i.e., all atomic columns show a black contrast. Such surface termination analysis is possible only if the TEM lamellae are prepared with care including healing out of surface oxygen loss, as reported by refs 28 and 42. The detailed procedure for TEM lamella preparation is summarized in the Methods section. All surfaces are studied after recrystallization in 1 mbar O_2 . The resulting trends in

surface termination of PCMO $x = 0.1$ and 0.33 epitaxially grown thin films in HV, O_2 , and H_2O are shown in Figure 2.

In HV, a quite ordered surface with mixed A-site (Pr/Ca–O) and B-site (Mn–O) terminated facets is observed for PCMO $x = 0.1$ (Figure 2a). In contrast, PCMO $x = 0.33$ shows a strongly disordered surface (Figure 2e) in HV. In 100 Pa O_2 , both PCMO $x = 0.1$ and $x = 0.33$ develop ordered surfaces with mixed A and B termination (Figure 2b,f). In H_2O , the surfaces exhibit again a pronounced disordered structure for both doping levels (Figure 2c for $x = 0.1$ at 0.8 Pa H_2O and Figure 2g for $x = 0.33$ at 0.5 Pa H_2O). For $x = 0.1$, there is a tendency that the A-site terminated facets are more ordered compared to the B-terminated facets. Figure 2d,h shows simulated images of PCMO $x = 0.1$ and $x = 0.33$, respectively. The simulated images refer to the [010] zone axis for PCMO $x = 0.1$ and the [110] zone axis for PCMO $x = 0.33$, both with [001] surfaces. The comparison of experimental images to simulations allows distinguishing the contrast of A-terminated and B-terminated facets for the [010] zone axis in Figure 2d, which is also visible in the experimental image in Figure 2c. For the [110] zone axis, the contrast difference between A and B layers is low. The amplitude oscillation of a MnO layer is only slightly lower than that for a Pr(Ca)O layer. However, based on the dynamical behavior, i.e., that Pr(Ca)O surfaces are much less dynamic than MnO surfaces, we suggest that the first disordered layer of the $x = 0.33$ system in H_2O in the initial state is mostly MnO terminated. The simulated images are obtained from multi-slice simulations using the QSTEM⁴⁵ software. The sample thickness as well as lens aberrations, i.e., defocus, spherical aberration, two-fold astigmatism, and axial coma, is fitted by minimizing the root-mean-square difference between experimental and simulated images as described in the Methods section.

Dynamical Disordered Surface Layer at the PCMO $x = 0.1$ – H_2O Interface. Figure 3a–d shows HRTEM images of PCMO $x = 0.1$ recorded in 0.8 Pa H_2O in ETEM taken from Movie M2 at different times. The frame rate of CCD is adjusted to 4 fps, which does not capture the entire surface dynamics but enables a sufficient signal-to-noise ratio to observe atomic contrast. The used frame rate gives only a lower limit to the adatom hopping rate on the surface, as demonstrated in our prior work.²⁸ Before we start the in situ observations in H_2O , the surface is fully recrystallized in 1 mbar O_2 (Movie M1 and Supporting Figure S3). Movie M3 shows increased adatom dynamics on the PCMO $x = 0.1$ (001) surface in 0.8 Pa H_2O (Supporting Figure S8) compared to that in O_2 (Supporting Figure S9 and Movie M1) or HV (Supporting Figure S10 and Movie M4). Interestingly, the disordered surface layer between the two crystalline facets shows more pronounced atom dynamics in the presence of H_2O compared to the ordered facets. This disordered layer does not grow over time. The two crystalline A-site terminated surface facets on each side of the disordered surface region remain stable and retain the perovskite structure even after 11 min. Consequently, PCMO $x = 0.1$ does not show irreversible structural degradation in contact with H_2O during the time of observation.

Dynamic PCMO $x = 0.33$ – H_2O Interface with Fast Mn Leaching. Figure 3e–h represents a time sequence of HRTEM images of the PCMO $x = 0.33$ (001) surface in 0.5 Pa H_2O in ETEM captured from Movies M5–M7. Before the study in H_2O , the lamella surface was completely recrystallized in 1 mbar O_2 (Figure 2f and Movie M8). In H_2O , the

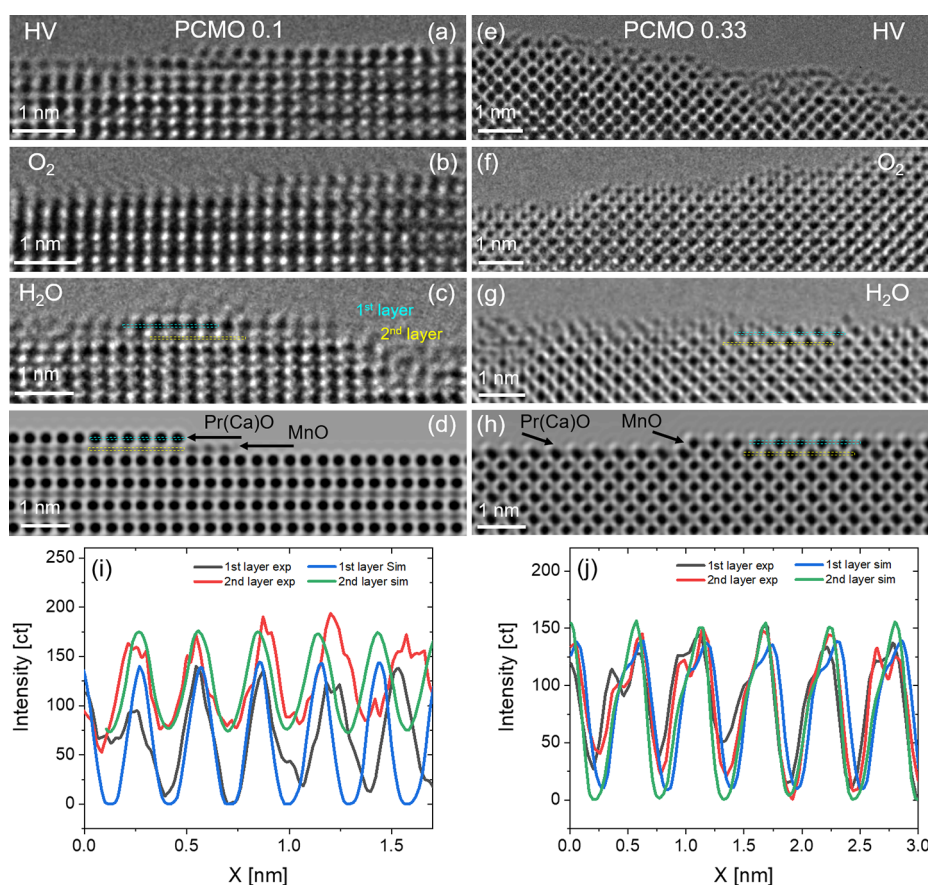


Figure 2. HRTEM images of PCMO (001) surfaces of $x = 0.1$ (left column) and 0.33 (right column) in different environments. (a–d) PCMO $x = 0.1$ is imaged in the [010] zone axis and (e–h) PCMO $x = 0.33$ in the [110] zone axis. (a) ($x = 0.1$) Mixed A and B termination in HV. (e) ($x = 0.33$) Disordered mixed A-site and B-site terminated surface in HV. (b) ($x = 0.1$) Dominant A-termination in 1 mbar O_2 . (f) ($x = 0.33$) More ordered probably mixed terminated surface in 1 mbar O_2 . (c) ($x = 0.1$) A-site terminated surface with a disordered layer in 0.8 Pa H_2O . (g) ($x = 0.33$) In H_2O , a more disordered surface develops, which consists probably of dynamic Mn on a more ordered Pr(Ca) layer. (d, h) Simulated images with mixed terminations for PCMO $x = 0.1$ and $x = 0.33$ surfaces, respectively. Panels (i) and (j) compare line profiles of the simulated contrast of the first and second layers with experimental contrast in H_2O .

fluctuating B-site atomic columns form a highly dynamic disordered layer on the surface, whereas the A-site subsurface layer remains ordered and stable (Figure 3e and Movie M5). Figure 3g,h shows the PCMO $x = 0.33$ surface after 3 min (Movie M6) and 11 min (Movie M7) of observation. After 3 min, significant leaching of Mn is already visible with the formation of a cubic Pr-rich bilayer surface. This process continues until the Pr-rich cubic phase forms up to a thickness of three to four monolayers (Figure 3h). Supporting Figure S11 shows the line profiles of the time evolution of the surface contrast as well as post-mortem EELS analysis, which reveals Pr and O edges, while the Mn L edge at 640 eV vanished below the noise level.

Dynamic (112) Surface of PCMO 0.1 with Oscillating Mn Column Occupation. Figure 4a shows a time sequence of HRTEM images with a temporally periodic surface reconstruction of a PCMO $x = 0.1$ (112) surface facet in 0.5 Pa H_2O , taken from Movie M9. This surface orientation intrinsically has a termination of alternating A and B columns. The dynamic surface reconstruction consists of an oscillatory variation of the occupancy of Mn–O columns in the [110] direction with Mn and O atoms, where columns become “less occupied” and “filled” again. In contrast, the A columns are more or less stable. Such an oscillatory behavior is absent in HV.

Figure 4b shows the line profile for the area marked by a dotted white rectangle in Figure 4a. Areas marked by three dotted yellow circles in the line profile indicate the 1, 2, and 3 B-site atomic columns that reveal an oscillating type of behavior in the line profile. In contrast to B sites, A sites marked by arrows in Figure 4a and in the line profile are stable for 10 min of observation. It is important to note that we do not observe Mn leaching out of the (112) surface at $x = 0.1$. Image simulation in Figure 4c,d reveals that the contrast variation of the B-site columns is consistent with oscillation between 100% and almost 0% filling. Altogether, the PCMO $x = 0.1$ (112) surface shows a highly dynamic oscillating surface reconstruction with remarkable stability on timescales of several minutes.

Movie M9 gives a larger overview area with mobile Mn atomic columns on the (112) surface. Here, additional dynamics of the monolayer step edges of the (112) surface are observed. It displays two different types of atom dynamics: a temporally oscillating surface reconstruction close to the step edges and a jumping-like displacement of entire Mn–O atomic columns. Probably, this is related to the B-site atomic columns’ fast oscillating behavior.

Change of the Oxidation State Close to the Surface. Figure 5 shows the EELS analysis of the PCMO $x = 0.1$ (001) surface. The O K and Mn L edges are recorded post O_2 (100

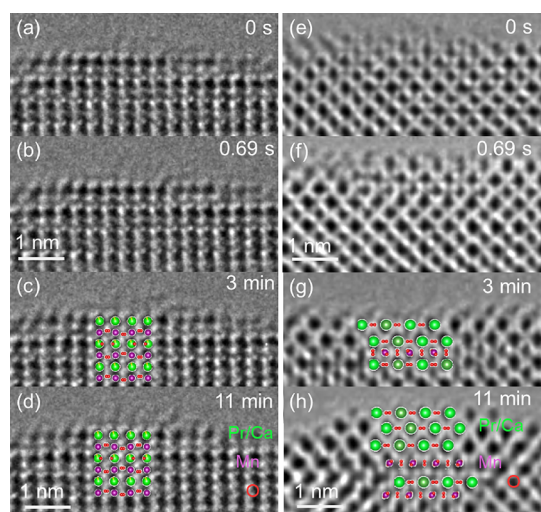


Figure 3. Time-resolved series of HRTEM images of PCMO (001) $x = 0.1$ and 0.33 surfaces at negative defocus that show atomic dynamics in H_2O . (a–d) HRTEM images captured from *Movie M2* recorded at 4 fps at the [010] zone axis for PCMO $x = 0.1$. The sequence shows stable A-site termination for a longer time in H_2O . The surface does not exhibit any structural changes and retains the perovskite structure even after 11 min. Mn adatoms show mobility on the surface from the beginning of the movie. (e) HRTEM image taken from a time series at a rate of 4 fps at the [110] zone axis for PCMO $x = 0.33$, compiled in *Movies M5–M7*. (f–h) Later stages of that surface area at the same conditions confirm Mn leaching from the topmost three atomic layers of the surface.

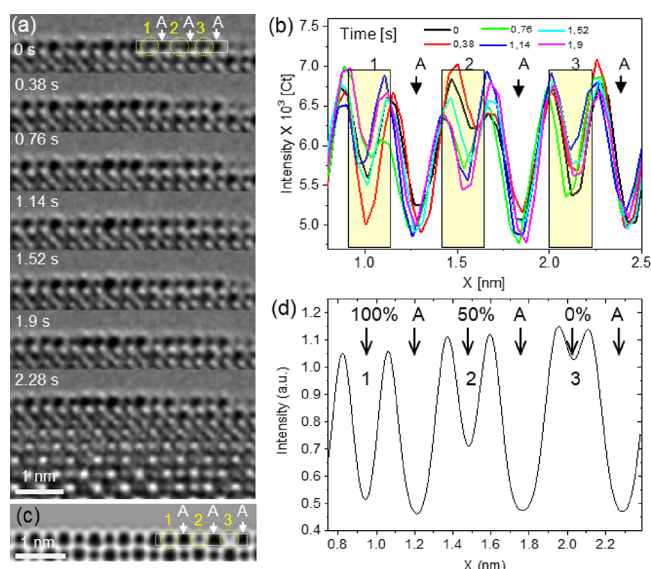


Figure 4. Time sequence of HRTEM images of the PCMO $x = 0.1$ (112) surface imaged in the [110] zone axis at negative defocus. (a) Series of HRTEM images captured at 3 fps from *Movie M9*. The HRTEM images are recorded in $0.5 \text{ Pa H}_2\text{O}$. At this surface orientation, alternating B- and A-site columns are observed at the surface. The B column show a temporally fluctuating contrast, whereas the A column is more stable. (b) Times series of the line profiles of the top layer at the surface marked by a white dotted rectangle in the 0 s HRTEM image in panel (a). Yellow rectangles in the line profile graph indicate the marked three Mn atomic columns. (c) Simulated contrast with the varying occupation of the B-site (MnO) columns as indicated in the line profiles in (d).

Pa) and post H_2O in HV (after removing O_2 and H_2O from ETEM). They are taken at the surface (black rectangle) and the bulk (red rectangle) of the TEM lamella, marked in the ADF-STEM image (Figure 5a,b). All of the high-loss spectra are energy calibrated using the corresponding zero-loss peak and then background subtracted as described in the Methods section. Figure 5c shows the O K edges that are mainly dominated by the three peaks labeled as a, b, and c and are typical of the perovskite structure. The prepeak at around 530 eV is attributed to the transition from the $1s$ oxygen core state to empty $2p$ states, which hybridize with Mn $3d$ orbitals. Peak b is associated with the A-site $5d$ orbitals/B-site $4sp$ orbitals, and peak c is related to the transition in the vacuum or due to multiple scattering of electronic excitations.^{47,48}

Figure 5d compares the Mn L_3 and L_2 edges from the surface and bulk of the post O_2 and post H_2O measurements. The energy position of Mn L edges as well as the intensity ratio of the L_2 and L_3 peaks reflects the Mn valence state in the PCMO $x = 0.1$ systems. The energy position of Mn L edges post O_2 and post H_2O shows slight changes at the surface. The tiny shift in the Mn L edges at the surface post H_2O indicates a decrease in the Mn valence state after the H_2O treatment in ETEM. This is also demonstrated by calculating the Mn valence using the integrated L_3/L_2 ratio, as shown in ref 44. Both PCMO systems show a slightly higher Mn valence in contact with a high partial pressure of O_2 (100 Pa) in ETEM. The resulting Mn valence is shown in Figure 5e (top). For $x = 0.1$, it is stable in the bulk and shows a very slight valence decrease from Mn $3.3+ (\pm 0.26)$ to Mn $3.1+ (\pm 0.1)$ at the surface after contact with H_2O ; however, it is within the error range. EELS analysis thus suggests that the oxidation state of Mn is more or less maintained for the $x = 0.1$ sample. This is in good agreement with the preservation of the perovskite structure observed in HRTEM images in H_2O . Post-mortem EELS analysis after $0.5 \text{ Pa H}_2\text{O}$ for PCMO $x = 0.33$ is described in ref 28. Here, the O K prepeak is substantially reduced after 12 min of contact with H_2O . The change in the Mn L edge, L_3/L_2 intensity ratio, and calculated Mn valence indicates a significant decrease in the Mn valence close to the surface ($\sim 2 \text{ nm}$) from $3.5+ (\pm 0.14)$ to $2.9+ (\pm 0.12)$ after $0.5 \text{ Pa H}_2\text{O}$ (Figure 5e, bottom). In contrast, in the pristine state of the TEM lamella, the Mn valence at the surface is maintained at a value of about 3.25 ; see Supporting Figure S12.

Figure 6 summarizes the Mn adatom and lattice Mn atomic column dynamics on (001) and (112) PCMO $x = 0.1$ surfaces recorded in the [010] and [110] zone axes, respectively. In Figure 6a, the fluctuating dynamics of Mn adatom columns are schematically depicted as suggested by the time series of HRTEM images of the (001) surface of PCMO $x = 0.1$. This is derived from *Movie M2* and the two HRTEM figures at 0 and 0.7 s to the right of the scheme. These HRTEM images clearly show fluctuating B-site contrast on a stable A-site terminated surface. This is most probably due to dynamic Mn adatoms. Figure 6b shows the oscillation of the occupation of an entire lattice Mn atomic column on the (112) surface as visible in Figure 4 and in the HRTEM images to the right of the scheme in Figure 6b. Such Mn atomic column dynamics are substantial in H_2O (see Supporting Figure S8) and decrease drastically in O_2 and HV environments (see Supporting Figures S9 and S10). Both the (001) and (112) surfaces thus show highly dynamic Mn species at the surface in the presence of H_2O . These dynamics are reversible in contrast to the leaching behavior of Mn for $x = 0.33$.

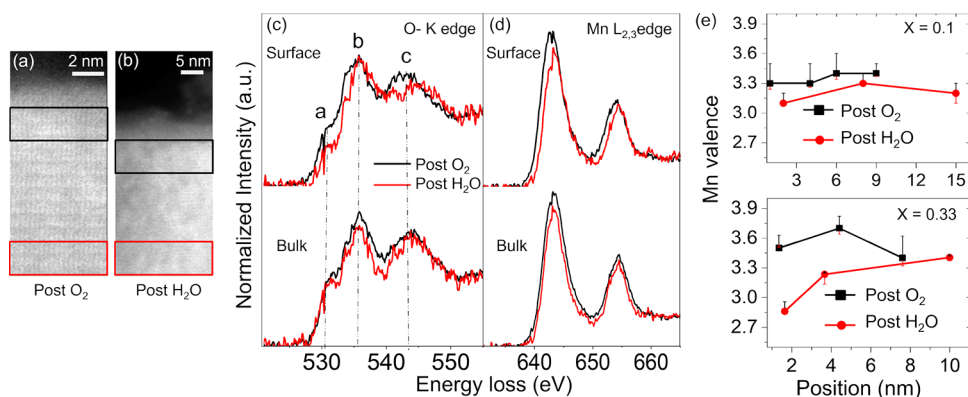


Figure 5. EELS analysis of the Mn L edge and O K edge of PCMO $x = 0.1$ at the surface and in the bulk in HV imaged after atomic dynamic observations in 100 Pa O_2 and 0.8 Pa H_2O , respectively. (a, b) ADF-STEM images of PCMO $x = 0.1$. The spectra of the (c) oxygen K edge and (d) Mn L edge are recorded in the area from the surface (black rectangle) and bulk (red rectangle) shown in panels (a) and (b). The Mn L edge show a small change after the H_2O treatment at the surface. A slight decrease in the O K prepeak at 531 eV indicates a minor surface reduction. Panel (e) shows that the Mn^{3+} valence is retained after contact with water for $x = 0.1$ and there is a significant decrease in Mn valence for $x = 0.33$.

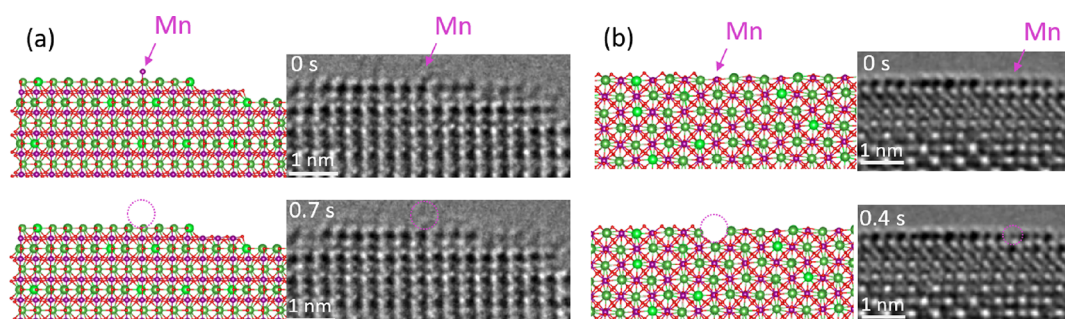


Figure 6. Atomic models and experimental images of the PCMO $x = 0.1$ (001) and (112) surfaces show different types of Mn dynamics. (a) Atomic model and experimental HRTEM images of the (001) surface of PCMO $x = 0.1$ in the $[010]$ zone axis. (b) (112) surface of PCMO $x = 0.1$ in the $[110]$ zone axis. The appearance and disappearance of Mn atomic columns are indicated by the pink arrow and dotted circle for both surfaces, respectively.

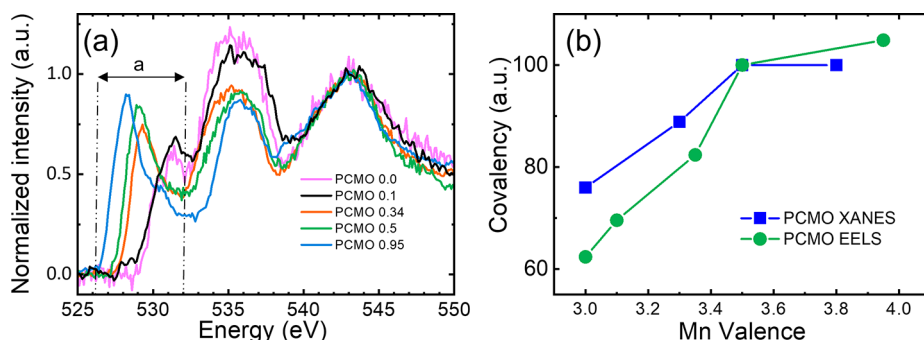


Figure 7. (a) EELS of the O K edge of PCMO $x = 0-0.95$ thin film lamellae. (b) Covalence analysis calculated from EELS analysis and X-ray absorption spectroscopy of the O K edge as a function of Mn valence.

In the following, we discuss the physical origin of the different behaviors of PCMO 0.1 and 0.33. Figure 7a shows EELS spectra of O K edges for PCMO with Ca doping of 0, 0.1, 0.34, 0.5, and 0.95. There is a strong increase in prepeak “a” intensity and a shift to lower energy with an increase in Ca doping. These trends are also seen in DFT calculations.⁴⁹ However, these changes cannot be solely attributed to the change of the e_g filling, i.e., Mn valence state. Furthermore, the degree of hybridization between Mn 3d states to O 2p states, i.e., covalence, is also modified. To analyze this effect, the prepeak area “a” in Figure 7a is used to calculate the experimental covalence factor for all doping levels. After proper

background subtraction and normalization, prepeak “a” is integrated from 529 to 532 eV and then divided by the change in the valence state.³⁵ All results are then normalized to the value at PCMO $x = 0.5$. Figure 7b shows the result, revealing an increase in hybridization with increasing Mn valence. The covalence change calculated by X-ray absorption near-edge spectroscopy³⁸ (XANES) shows a similar trend (Figure 7b, blue line).

PCMO shows Jahn–Teller polarons at both doping levels, i.e., small polarons that show hopping conductivity.^{50,51} Since acceptor states for electrons from water oxidation are formed by the Jahn–Teller split empty states, i.e., Mn 3d e_g

antibonding states, we conclude that these acceptor states also have a small polaron type of character in the studied doping range. Consequently, electrons from water oxidation are rather localized, and the degree of localization depends on the covalence. In PCMO $x = 0.33$, the higher covalence, i.e., the higher hybridization of Mn 3d and O 2p, gives rise to a pronounced Zener polaron physics. Here, Jahn–Teller polarons are ferromagnetically coupled via the oxygen bridge.^{49,52} This has the consequence that additional electrons in Mn 3d acceptor states can easily reduce lattice oxygen, forming O⁻ and even neutral O charge states, which can lead to O₂(g) and pronounced oxygen vacancy formation. In contrast, for PCMO $x = 0.1$, such Zener polaron physics is less pronounced, and the additional electrons in the 3d e_g acceptor states can only move between different Mn sites via thermally active polaron hopping.

Thus, despite the change in the e_g filling, the main difference between the two doping levels is a change in the overlap of the Mn 3d e_g states with the O 2p states. This can be quantified by the covalence factor, as shown in ref 53. We follow the method as described in ref 35, revealing a reduced covalency for the $x = 0.1$ system compared to that for $x = 0.33$. Although the atomic structure at the surface is different from that in the bulk, our argument is relevant, since the subsurface layer is important for acquisition of the electrons from surface acceptor states. Furthermore, oxygen vacancy formation in the subsurface is essential for the observed irreversible processes of Mn reduction and leaching in the $x = 0.33$ system.

CONCLUSIONS

In summary, we discovered distinct behaviors of manganite (001) surfaces for OER with different A-site dopings. As more extensively analyzed in a previous work,²⁸ PCMO $x = 0.33$ shows the formation of Mn²⁺ species, which can leach out of the electrode surface. This is due to subsurface oxygen vacancy formation. The resulting reduced Mn species have a high solubility in H₂O. In contrast, O K and Mn L edges in EELS analysis confirm the stable Mn valence at the PCMO $x = 0.1$ (001) surface. We have repeated the experiments on the formation of a Pr-rich cubic phase at the subsurface of the PCMO $x = 0.33$ system, which is fully consistent with the results in ref 28.

Similar to cobaltates, where the enhancement in the TM 3d–O 2p covalence facilitates the charge transfer between the occupied O 2p and unoccupied TM 3d states and increases OER activity,^{34,54} the PCMO $x = 0.33$ system shows a higher initial OER activity. However, it experiences fast corrosion on the surface and thus represents an unstable system for OER. In contrast, PCMO $x = 0.1$ (001) and (112) surfaces show pronounced reversible Mn surface dynamics in H₂O. These surfaces possess higher stability both in ETEM and in RRDE studies under conditions that facilitate surface reduction, i.e., in O₂-poor environments and at moderate anodic polarization. In particular, the in situ ETEM experiments do not reveal any hint of irreversible Mn leaching out of the PCMO $x = 0.1$ interface to H₂O.

Even though PCMO is not among the top catalysts for OER, this study gives new insights about the role of the covalence factor and charge localization. Charge localization in e_g acceptor states due to polaron formation is not itself detrimental to electrode stability, which depends on hybridization to O 2p states. The latter facilitates lattice oxygen reduction and subsequent vacancy formation. Thus, this

phenomenon can lead to the local reduction of surface Mn. Remarkably, high stability and high activity are observed for the (La,Sr)MnO₃ system in the ferromagnetic metallic state, where acceptor states are delocalized to varying degrees.^{28,46} Here, electrons from H₂O oxidation form band-like carriers and lattice oxygen reduction is absent. This suggests that perovskite oxides with simultaneously high activity and stability are based on the requirement that oxidation of lattice oxygen due to a strong covalence of localized charges needs to be avoided. In the case of PCMO $x = 0.1$, localized Mn 3d e_g charges due to small polaron formation have a lower overlap with the O 2p states reflected by the smaller covalency.

ASSOCIATED CONTENT

Supporting Information

The Supporting Information is available free of charge at <https://pubs.acs.org/doi/10.1021/acs.jpcc.2c05622>.

AFM images of as-grown epitaxial PCMO $x = 0.1$ (001) and PCMO $x = 0.33$ (001) thin films; logarithmically plotted XRD patterns of epitaxially grown PCMO $x = 0.1$ and $x = 0.33$ thin films; cyclic voltammograms of the thin film disk and the corresponding ring current; chronoamperometric measurements for PCMO $x = 0.1$ and $x = 0.33$ epitaxial films at different applied potentials as a function of time in an argon-saturated electrolyte; chronoamperometric measurements at different applied potentials as a function of time in an O₂-saturated electrolyte; TEM lamella preparation; HRTEM images of the as-prepared and recrystallized surfaces for PCMO $x = 0.1$; time sequence of HRTEM frames for PCMO $x = 0.1$ in HV, O₂, and H₂O; time sequence of HRTEM frames for PCMO $x = 0.33$ in H₂O and post-mortem EELS; EELS of the pristine state of the PCMO 0.33 lamella; image simulation parameters; details of supporting movies (PDF)

Supporting movies showing a highly ordered Pr_{0.9}Ca_{0.1}MnO₃ surface, a dynamic surface in contact with H₂O, Mn adatoms fluctuations on a stable A-site terminated surface, mixed surface termination, a perovskite structure before Mn leaching, slow Mn leaching from the first two layers after 3 min, progressed leaching of Mn from the surface after 11 min, a highly ordered Pr_{0.67}Ca_{0.33}MnO₃ surface, and the oscillatory behavior of Mn atomic columns at the (112) surface (ZIP)

AUTHOR INFORMATION

Corresponding Author

Christian Jooss – *Institute of Materials Physics, University of Goettingen, 37077 Goettingen, Germany; International Center for Advanced Studies of Energy Conversion (ICASEC), University of Goettingen, D-37077 Goettingen, Germany; orcid.org/0000-0002-8762-9359; Phone: +49 551 3925303; Email: cjooss@gwdg.de*

Authors

Gaurav Lole – *Institute of Materials Physics, University of Goettingen, 37077 Goettingen, Germany; International Center for Advanced Studies of Energy Conversion (ICASEC), University of Goettingen, D-37077 Goettingen, Germany; orcid.org/0000-0001-9227-8752*

Fatemeh Ebrahimi – *Institute of Materials Physics, University of Goettingen, 37077 Goettingen, Germany; Present*

Address: Institut für Optische und Elektronische Materialien, Technical University of Hamburg, D-21073 Hamburg, Germany (F.E.); orcid.org/0000-0002-2532-5691

Tobias Meyer – Institute of Materials Physics, University of Goettingen, 37077 Goettingen, Germany; orcid.org/0000-0003-3191-0376

Daniel Mierwaldt – Institute of Materials Physics, University of Goettingen, 37077 Goettingen, Germany

Vladimir Roddatis – Institute of Materials Physics, University of Goettingen, 37077 Goettingen, Germany; Present Address: Helmholtz-Zentrum Potsdam Deutsches GeoForschungsZentrum GFZ, Telegrafenberg, 14473 Potsdam, Germany (V.R.).

Janis Geppert – Institute of Materials Physics, University of Goettingen, 37077 Goettingen, Germany; Present Address: Institute for Applied Materials – Electrochemical Technologies, Karlsruhe Institute of Technology, Adenauerring 20b, 76131 Karlsruhe, Germany (J.G.); orcid.org/0000-0002-9991-2725

Marcel Risch – Institute of Materials Physics, University of Goettingen, 37077 Goettingen, Germany; Young Investigator Group Oxygen Evolution Mechanism Engineering, Helmholtz-Zentrum Berlin für Materialien und Energie GmbH, 14109 Berlin, Germany; orcid.org/0000-0003-2820-7006

Complete contact information is available at: <https://pubs.acs.org/10.1021/acs.jpcc.2c05622>

Author Contributions

G.L., T.M., D.M., and V.R. performed the TEM experiments. G.L. analyzed the TEM data. J.G. prepared the manganite thin films. F.E. and J.G. did the electrochemical measurements. M.R. and C.J. contributed to their analysis. T.M. did image simulation. C.J. supervised the work. All authors contributed to the writing of the manuscript.

Notes

The authors declare no competing financial interest.

ACKNOWLEDGMENTS

This work is financially funded by DFG 217133147/SFB 1073 project C02. The “Collaborative Laboratory and User Facility for Electron Microscopy” (CLUE) at the University of Goettingen is acknowledged for instrumentation support.

REFERENCES

- (1) Liu, D.; Zhou, P.; Bai, H.; Ai, H.; Du, X.; Chen, M.; Liu, D.; Fai Ip, W.; Ho Lo, K.; Tat Kwok, C.; Chen, S.; Wang, S.; Xing, G.; Wang, X.; Pan, H.; Liu, D.; Zhou, P.; Bai, H.; Chen, M.; Chen, S.; Wang, S.; Xing, G.; Pan, H.; Ai, H.; Du, X.; Lo, K. H.; Kwok, C. T.; Ip, W. F.; Wang, X. Development of Perovskite Oxide-Based Electrocatalysts for Oxygen Evolution Reaction. *Small* **2021**, *17*, 2101605.
- (2) She, S.; Zhu, Y.; Tahini, H. A.; Hu, Z.; Weng, S.-C.; Wu, X.; Chen, Y.; Guan, D.; Song, Y.; Dai, J.; Smith, S. C.; Wang, H.; Zhou, W.; Shao, Z. A Molecular-Level Strategy to Boost the Mass Transport of Perovskite Electrocatalyst for Enhanced Oxygen Evolution. *Appl. Phys. Rev.* **2021**, *8*, No. 011407.
- (3) Edgington, J.; Schweitzer, N.; Alayoglu, S.; Seitz, L. C. Constant Change: Exploring Dynamic Oxygen Evolution Reaction Catalysis and Material Transformations in Strontium Zinc Iridate Perovskite in Acid. *J. Am. Chem. Soc.* **2021**, *143*, 9961–9971.
- (4) Fu, G.; Li, W.; Zhang, J.-Y.; Li, M.; Li, C.; Li, N.; He, Q.; Xi, S.; Qi, D.; MacManus-Driscoll, J. L.; Cheng, J.; Zhang, K. H. Facilitating the Deprotonation of OH to O through Fe⁴⁺-Induced States in

Perovskite LaNiO₃ Enables a Fast Oxygen Evolution Reaction. *Small* **2021**, *17*, 2006930.

(5) Man, I. C.; Su, H. Y.; Calle-Vallejo, F.; Hansen, H. A.; Martínez, J. I.; Inoglu, N. G.; Kitchin, J.; Jaramillo, T. F.; Nørskov, J. K.; Rossmeisl, J. Universality in Oxygen Evolution Electrocatalysis on Oxide Surfaces. *ChemCatChem* **2011**, *3*, 1159–1165.

(6) Porokhin, S. V.; Nikitina, V. A.; Aksyonov, D. A.; Filimonov, D. S.; Pazhetnov, E. M.; Mikheev, I. V.; Abakumov, A. M. Mixed-Cation Perovskite La_{0.6}Ca_{0.4}Fe_{0.7}Ni_{0.3}O_{2.9} as a Stable and Efficient Catalyst for the Oxygen Evolution Reaction. *ACS Catal.* **2021**, *11*, 8338–8348.

(7) Retuerto, M.; Pascual, L.; Piqué, O.; Kayser, P.; Salam, M. A.; Mokhtar, M.; Alonso, J. A.; Peña, M.; Calle-Vallejo, F.; Rojas, S. How Oxidation State and Lattice Distortion Influence the Oxygen Evolution Activity in Acid of Iridium Double Perovskites. *J. Mater. Chem. A* **2021**, *9*, 2980–2990.

(8) Quinn Carvalho, O.; Adiga, P.; Wang, L.; Liu, J.; Jia, E.; Du, Y.; NemšákNemšák, S.; Stoerzinger, K. A. Probing Adsorbates on La_{1-x}Sr_xNiO_{3-δ} Surfaces under Humid Conditions: Implications for the Oxygen Evolution Reaction. *J. Phys. D: Appl. Phys.* **2021**, *54*, 274003.

(9) Yun, T. G.; Heo, Y.; Bin Bae, H.; Chung, S.-Y. Elucidating Intrinsic Contribution of D-Orbital States to Oxygen Evolution Electrocatalysis in Oxides. *Nat. Commun.* **2021**, *12*, 1–11.

(10) Lin, Y.; Tian, Z.; Zhang, L.; Ma, J.; Jiang, Z.; Deibert, B. J.; Ge, R.; Chen, L. Chromium-Ruthenium Oxide Solid Solution Electrocatalyst for Highly Efficient Oxygen Evolution Reaction in Acidic Media. *Nat. Commun.* **2019**, *10*, 1.

(11) Reier, T.; Nong, H. N.; Teschner, D.; Schlögl, R.; Strasser, P. Electrocatalytic Oxygen Evolution Reaction in Acidic Environments – Reaction Mechanisms and Catalysts. *Adv. Energy Mater.* **2017**, *7*, 1601275.

(12) Escalera-López, D.; Czioska, S.; Geppert, J.; Boubnov, A.; Röse, P.; Saraçi, E.; Krewer, U.; Grunwaldt, J. D.; Cherevko, S. Phase- and Surface Composition-Dependent Electrochemical Stability of Ir-Ru Nanoparticles during Oxygen Evolution Reaction. *ACS Catal.* **2021**, *11*, 9300–9316.

(13) Ledendecker, M.; Geiger, S.; Hengge, K.; Lim, J.; Cherevko, S.; Mingers, A. M.; Göhl, D.; Fortunato, G. V.; Jalalpoor, D.; Schüth, F.; Scheu, C.; Mayrhofer, K. J. J. Towards Maximized Utilization of Iridium for the Acidic Oxygen Evolution Reaction. *Nano Res.* **2019**, *12*, 2275–2280.

(14) She, Z. W.; Kibsgaard, J.; Dickens, C. F.; Chorkendorff, I. B.; Nørskov, J. K.; Jaramillo, T. F. Combining Theory and Experiment in Electrocatalysis: Insights into Materials Design. *Science* **2017**, *355*, No. eaad4998.

(15) Song, F.; Bai, L.; Moysiadou, A.; Lee, S.; Hu, C.; Liardet, L.; Hu, X. Transition Metal Oxides as Electrocatalysts for the Oxygen Evolution Reaction in Alkaline Solutions: An Application-Inspired Renaissance. *J. Am. Chem. Soc.* **2018**, *140*, 7748–7759.

(16) Roger, I.; Shipman, M. A.; Symes, M. D. Earth-Abundant Catalysts for Electrochemical and Photoelectrochemical Water Splitting. *Nat. Rev. Chem.* **2017**, *1*, 1–13.

(17) Zhao, J.-W.; Shi, Z.-X.; Li, C.-F.; Gu, L.-F.; Li, G.-R. Boosting the Electrocatalytic Performance of NiFe Layered Double Hydroxides for the Oxygen Evolution Reaction by Exposing the Highly Active Edge Plane (012). *Chem. Sci.* **2021**, *12*, 650–659.

(18) Yin, W.-J.; Weng, B.; Ge, J.; Sun, Q.; Li, Z.; Yan, Y. Oxide Perovskites, Double Perovskites and Derivatives for Electrocatalysis, Photocatalysis, and Photovoltaics. *Energy Environ. Sci.* **2019**, *12*, 442–462.

(19) Wang, W.; Xu, M.; Xu, X.; Zhou, W.; Shao, Z. Perovskite Oxide Based Electrodes for High-Performance Photoelectrochemical Water Splitting. *Angew. Chem., Int. Ed.* **2020**, *59*, 136–152.

(20) Zhao, J.-W.; Shi, Z.-X.; Li, C.-F.; Ren, Q.; Li, G.-R. Regulation of Perovskite Surface Stability on the Electrocatalysis of Oxygen Evolution Reaction. *ACS Mater. Lett.* **2021**, *3*, 721–737.

(21) Dong, F.; Li, L.; Kong, Z.; Xu, X.; Zhang, Y.; Gao, Z.; Dongyang, B.; Ni, M.; Liu, Q.; Lin, Z. Materials Engineering in

- Perovskite for Optimized Oxygen Evolution Electrocatalysis in Alkaline Condition. *Small* **2021**, *17*, 2006638.
- (22) Nguyen, T. X.; Liao, Y.-C.; Lin, C.-C.; Su, Y.-H.; Ting, J.-M. Advanced High Entropy Perovskite Oxide Electrocatalyst for Oxygen Evolution Reaction. *Adv. Funct. Mater.* **2021**, *31*, 2101632.
- (23) Peng, M.; Huang, J.; Zhu, Y.; Zhou, H.; Hu, Z.; Liao, Y.-K.; Lai, Y.-H.; Chen, C.-T.; Chu, Y.-H.; Zhang, K. H. L.; Fu, X.; Zuo, F.; Li, J.; Sun, Y. Structural Anisotropy Determining the Oxygen Evolution Mechanism of Strongly Correlated Perovskite Nickelate Electrocatalyst. *ACS Sustainable Chem. Eng.* **2021**, *9*, 4262–4270.
- (24) Chen, Y.; Li, H.; Wang, J.; Du, Y.; Xi, S.; Sun, Y.; Sherburne, M.; Ager, J. W.; Fisher, A. C.; Xu, Z. J. Exceptionally Active Iridium Evolved from a Pseudo-Cubic Perovskite for Oxygen Evolution in Acid. *Nat. Commun.* **2019**, *10*, 1–10.
- (25) Risch, M.; Grimaud, A.; May, K. J.; Stoerzinger, K. A.; Chen, T. J.; Mansour, A. N.; Shao-Horn, Y. Structural Changes of Cobalt-Based Perovskites upon Water Oxidation Investigated by EXAFS. *J. Phys. Chem. C* **2013**, *117*, 8628–8635.
- (26) May, K. J.; Carlton, C. E.; Stoerzinger, K. A.; Risch, M.; Suntivich, J.; Lee, Y. L.; Grimaud, A.; Shao-Horn, Y. Influence of Oxygen Evolution during Water Oxidation on the Surface of Perovskite Oxide Catalysts. *J. Phys. Chem. Lett.* **2012**, *3*, 3264–3270.
- (27) Fabbri, E.; Nachtegaal, M.; Binninger, T.; Cheng, X.; Kim, B. J.; Durst, J.; Bozza, F.; Graule, T.; Schäublin, R.; Wiles, L.; Pertoso, M.; Danilovic, N.; Ayers, K. E.; Schmidt, T. J. Dynamic Surface Self-Reconstruction Is the Key of Highly Active Perovskite Nano-Electrocatalysts for Water Splitting. *Nat. Mater.* **2017**, *16*, 925–931.
- (28) Lole, G.; Roddatis, V.; Ross, U.; Risch, M.; Meyer, T.; Rump, L.; Geppert, J.; Wartner, G.; Blöchl, P.; Jooss, C. Dynamic Observation of Manganese Adatom Mobility at Perovskite Oxide Catalyst Interfaces with Water. *Commun. Mater.* **2020**, *1*, 68.
- (29) Yoo, J. S.; Rong, X.; Liu, Y.; Kolpak, A. M. Role of Lattice Oxygen Participation in Understanding Trends in the Oxygen Evolution Reaction on Perovskites. *ACS Catal.* **2018**, *8*, 4628–4636.
- (30) Grimaud, A.; Diaz-Morales, O.; Han, B.; Hong, W. T.; Lee, Y.-L.; Giordano, L.; Stoerzinger, K. A.; Koper, M. T. M.; Shao-Horn, Y. Activating Lattice Oxygen Redox Reactions in Metal Oxides to Catalyze Oxygen Evolution. *Nat. Chem.* **2017**, *9*, 457–465.
- (31) Man, I. C.; Su, H. Y.; Calle-Vallejo, F.; Hansen, H. A.; Martínez, J. I.; Inoglu, N. G.; Kitchin, J.; Jaramillo, T. F.; Nørskov, J. K.; Rossmeisl, J. Universality in Oxygen Evolution Electrocatalysis on Oxide Surfaces. *ChemCatChem* **2011**, *3*, 1159–1165.
- (32) Suntivich, J.; May, K. J.; Gasteiger, H. A.; Goodenough, J. B.; Shao-Horn, Y. A Perovskite Oxide Optimized for Oxygen Evolution Catalysis from Molecular Orbital Principles. *Science* **2011**, *334*, 1383–1385.
- (33) Zhang, Y.; Sun, Y.-F.; Luo, J.-L.; Kim, B.; Fabbri, E.; Antipin, D.; Risch, M. Trends of Epitaxial Perovskite Oxide Films Catalyzing the Oxygen Evolution Reaction in Alkaline Media. *J. Phys. Energy* **2020**, *2*, No. 032003.
- (34) Heymann, L.; Weber, M. L.; Wohlgemuth, M.; Risch, M.; Dittmann, R.; Baeumer, C.; Gunkel, F. Separating the Effects of Band Bending and Covalency in Hybrid Perovskite Oxide Electrocatalyst Bilayers for Water Electrolysis. *ACS Appl. Mater. Interfaces* **2022**, *14*, 14129–14136.
- (35) Abrishami, M. E.; Risch, M.; Scholz, J.; Roddatis, V.; Osterthun, N.; Jooss, C. Oxygen Evolution at Manganite Perovskite Ruddlesden-Popper Type Particles: Trends of Activity on Structure, Valence and Covalence. *Materials* **2016**, *9*, 921.
- (36) Song, J.; Wei, C.; Huang, Z.-F.; Liu, C.; Zeng, L.; Wang, X.; Xu, Z. J. A Review on Fundamentals for Designing Oxygen Evolution Electrocatalysts. *Chem. Soc. Rev.* **2020**, *49*, 2196.
- (37) Raabe, S.; Mierwaldt, D.; Ciston, J.; Uijtewaal, M.; Stein, H.; Hoffmann, J.; Zhu, Y.; Blöchl, P.; Jooss, C. In Situ Electrochemical Electron Microscopy Study of Oxygen Evolution Activity of Doped Manganite Perovskites. *Adv. Funct. Mater.* **2012**, *22*, 3378–3388.
- (38) Mierwaldt, D.; Mildner, S.; Arrigo, R.; Knop-Gericke, A.; Franke, E.; Blumenstein, A.; Hoffmann, J.; Jooss, C. In Situ XANES/XPS Investigation of Doped Manganese Perovskite Catalysts. *Catalysts* **2014**, *4*, 129–145.
- (39) Forslund, R. P.; Hardin, W. G.; Rong, X.; Abakumov, A. M.; Filimonov, D.; Alexander, C. T.; Mefford, J. T.; Iyer, H.; Kolpak, A. M.; Johnston, K. P.; Stevenson, K. J. Exceptional Electrocatalytic Oxygen Evolution via Tunable Charge Transfer Interactions in $\text{La}_{0.5}\text{Sr}_{1.5}\text{Ni}_{1-x}\text{Fe}_x\text{O}_{4\pm\delta}$ Ruddlesden-Popper Oxides. *Nat. Commun.* **2018**, *9*, 1–11.
- (40) Crozier, P. A.; Hansen, T. W. In Situ and Operando Transmission Electron Microscopy of Catalytic Materials. *MRS Bull.* **2015**, *40*, 38–45.
- (41) Mildner, S.; Beleggia, M.; Mierwaldt, D.; Hansen, T. W.; Wagner, J. B.; Yazdi, S.; Kasama, T.; Ciston, J.; Zhu, Y.; Jooss, C. Environmental TEM Study of Electron Beam Induced Electrochemistry of $\text{Pr}_{0.64}\text{Ca}_{0.36}\text{MnO}_3$ Catalysts for Oxygen Evolution. *J. Phys. Chem. C* **2015**, *119*, 5301–5310.
- (42) Roddatis, V.; Lole, G.; Jooss, C. In Situ Preparation of $\text{Pr}_{1-x}\text{Ca}_x\text{MnO}_3$ and $\text{La}_{1-x}\text{Sr}_x\text{MnO}_3$ Catalysts Surface for High-Resolution Environmental Transmission Electron Microscopy. *Catalysts* **2019**, *9*, 751.
- (43) Crozier, P. A.; Chenna, S. In Situ Analysis of Gas Composition by Electron Energy-Loss Spectroscopy for Environmental Transmission Electron Microscopy. *Ultramicroscopy* **2011**, *111*, 177–185.
- (44) Varela, M.; Oxley, M. P.; Luo, W.; Tao, J.; Watanabe, M.; Lupini, A. R.; Pantelides, S. T.; Pennycook, S. J. Atomic-Resolution Imaging of Oxidation States in Manganites. *Phys. Rev. B* **2009**, *79*, No. 085117.
- (45) Koch, C. Determination of Core Structure Periodicity and Point Defect Along Dislocations; Ph.D. Thesis, Arizona State University, Tempe, AZ, 2002.
- (46) Scholz, J.; Risch, M.; Stoerzinger, K. A.; Wartner, G.; Shao-Horn, Y.; Jooss, C. Rotating Ring-Disk Electrode Study of Oxygen Evolution at a Perovskite Surface: Correlating Activity to Manganese Concentration. *J. Phys. Chem. C* **2016**, *120*, 27746–27756.
- (47) Kurata, H.; Colliex, C. Electron-Energy-Loss Core-Edge Structures in Manganese Oxides. *Phys. Rev. B* **1993**, *48*, 2102.
- (48) Du, G. H.; Yuan, Z. Y.; Van Tendeloo, G. Transmission Electron Microscopy and Electron Energy-Loss Spectroscopy Analysis of Manganese Oxide Nanowires. *Appl. Phys. Lett.* **2005**, *86*, 063113.
- (49) Sotoudeh, M.; Rajpurohit, S.; Blöchl, P.; Mierwaldt, D.; Norpoth, J.; Roddatis, V.; Mildner, S.; Kressdorf, B.; Iffland, B.; Jooss, C. Electronic Structure of $\text{Pr}_{1-x}\text{Ca}_x\text{MnO}_3$. *Phys. Rev. B* **2017**, *95*, No. 235150.
- (50) Hoffmann, J.; Moschkau, P.; Mildner, S.; Norpoth, J.; Jooss, C.; Wu, L.; Zhu, Y. Effects of Interaction and Disorder on Polarons in Colossal Resistance Manganite $\text{Pr}_{0.68}\text{Ca}_{0.32}\text{MnO}_3$ Thin Films. *Mater. Res. Express* **2014**, *1*, 46403.
- (51) Kressdorf, B.; Meyer, T.; Brink, M. T.; Seick, C.; Melles, S.; Ottinger, N.; Titze, T.; Meer, H.; Weisser, A.; Hoffmann, J.; Mathias, S.; Ulrichs, H.; Steil, D.; Seibt, M.; Blöchl, P. E.; Jooss, C. Orbital-Order Phase Transition in $\text{Pr}_{1-x}\text{Ca}_x\text{MnO}_3$ probed by photovoltaics. *Phys. Rev. B* **2021**, *103*, No. 235122.
- (52) Raiser, D.; Mildner, S.; Iffland, B.; Sotoudeh, M.; Blöchl, P.; Teichert, S.; Jooss, C. Evolution of Hot Polaron States with a Nanosecond Lifetime in a Manganite Perovskite. *Adv. Energy Mater.* **2017**, *7*, 1602174.
- (53) Suntivich, J.; Hong, W. T.; Lee, Y. L.; Rondinelli, J. M.; Yang, W.; Goodenough, J. B.; Dabrowski, B.; Freeland, J. W.; Shao-Horn, Y. Estimating Hybridization of Transition Metal and Oxygen States in Perovskites from $o\ k$ -Edge X-Ray Absorption Spectroscopy. *J. Phys. Chem. C* **2014**, *118*, 1856–1863.
- (54) Zhou, Y.; Sun, S.; Song, J.; Xi, S.; Chen, B.; Du, Y.; Fisher, A. C.; Cheng, F.; Wang, X.; Zhang, H.; Xu, Z. J.; Zhou, Y.; Sun, S.; Song, J.; Chen, B.; Zhang, H.; Xu, Z. J.; Xi, S.; Du, Y.; Fisher, A. C.; Cheng, F.; Wang, X. Enlarged Co-O Covalency in Octahedral Sites Leading to Highly Efficient Spinel Oxides for Oxygen Evolution Reaction. *Adv. Mater.* **2018**, *30*, 1802912.